JACS
JOURNAL OF THE AMERICAN CHEMICAL SOCIETY

Article

pubs.acs.org/JACS

Control and Impact of the Nanoscale Distribution of Supported Cobalt Particles Used in Fischer–Tropsch Catalysis

Peter Munnik, Petra E. de Jongh, and Krijn P. de Jong*

Inorganic Chemistry and Catalysis, Debye Institute for Nanomaterials Science, Utrecht University, Universiteitsweg 99, 3584 CG Utrecht, The Netherlands

Supporting Information

ABSTRACT: The proximity of nanoparticles may affect the performance, in particular the stability, of supported metal catalysts. Short interparticle distances often arise during catalyst preparation by formation of aggregates. The cause of aggregation of cobalt nanoparticles during the synthesis of highly loaded silica-supported catalysts was found to originate from the drying process after impregnation of the silica grains with an aqueous cobalt nitrate precursor. Maximal spacing of the Co_3O_4 nanoparticles was obtained by fluid-bed drying at 100 °C in a N_2 flow. Below this temperature, redistribution of liquid occurred before and during precipitation of a solid phase, leading to aggregation of the cobalt particles. At higher temperatures, nucleation and growth of Co_3O_4 occurred during the drying process also giving rise to aggregation. Fischer–Tropsch catalysis performed under industrially relevant conditions for unpromoted and Pt-promoted cobalt catalysts revealed that the size of aggregates (13–80 nm) of Co particles (size ∼9 nm) had little effect on activity. Large aggregates exhibited higher selectivities to long chain alkanes, possibly related to higher olefin formation with subsequent readsorption and secondary chain growth. Most importantly, larger aggregates of Co particles gave rise to extensive migration of cobalt (up to 75%) to the external surface of the macroscopic catalyst grains (38–75 μm). Although particle size did not increase inside the silica support grains, migration of cobalt to the external surface partly led to particle growth, thus causing a loss of activity. This cobalt migration over macroscopic length scales was suppressed by maximizing the distance between nanoparticles over the support. Clearly, the nanoscale distribution of particles is an important design parameter of supported catalysts in particular and functional nanomaterials in general.

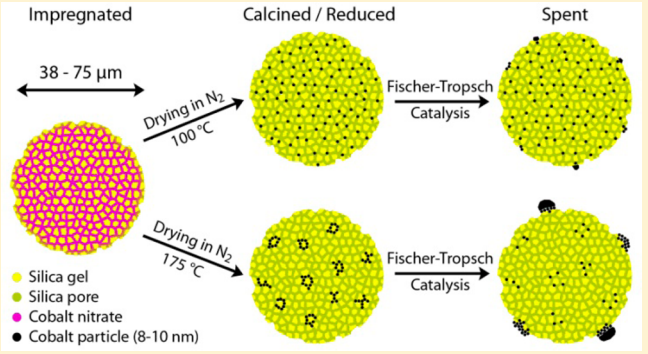

INTRODUCTION

Supported metal nanoparticles are at the center of many existing as well as new and more sustainable processes, such as energy conversion and storage, nanoelectronics, and the catalytic production of fuels and chemicals.[1−3] Unfortunately, degradation of these functional nanomaterials during usage is a major concern. Small metal particles often grow to larger crystals, either via particle migration and coalescence or through Ostwald ripening, whereby monomeric species are transported from small to large particles.[4−7] In specific cases crystal growth might be moderated by tuning properties of the nanoparticles such as their size,[8] composition,[9] and interaction with the support.[10] Particles being close together may lead to increased deactivation,[11] and recently, the interparticle distance was shown to have a large effect on the stability of copper catalysts for methanol synthesis.[12] However, the nanoscale distribution of particles is rarely studied and difficult to control. It has been noted that many materials, used both in academic and industrial context, exhibit nonuniform distributions of metal particles grouped together on the support as so-called aggregates or clusters of nanoparticles.[13−15]

Aggregates are often formed during the synthesis of the desired supported nanoparticles. Here we consider a widely used method of synthesis, impregnation of macroscopic support grains, followed by drying and subsequent thermal decomposition. Research has focused on circumventing the formation of aggregates through the choice of precursor,[16−18] addition of organic additives,[19−22] and changing the solvent.[23,24] However, systematic knowledge of aggregate formation of nanoparticles is lacking. The drying step has long been known to have a large impact on the macroscale distribution,[25,26] while recently it was also shown to have a large impact on the nanoscale distribution by studying conventional drying versus freeze-drying.[27−29]

Cobalt catalysts are often used for Fischer–Tropsch synthesis, whereby CO and H_2 are converted into long chain alkanes for the production of ultraclean transportation fuels. For industrial applications, the deactivation of these catalysts is a large problem.[30−35] However, the role of aggregation of nanoparticles on performance in general, and stability in

Received: January 15, 2014
Published: May 6, 2014

   dx.doi.org/10.1021/ja500436y | J. Am. Chem. Soc. 2014, 136, 7333−7340

particular, is not well-known. Changes in selectivities to long chain alkanes have been reported for catalysts with different degrees of aggregation, but this was always accompanied by a change in cobalt particle size,[36,37] support pore size,[38] support type,[39] or promoter addition,[40] factors which can also influence the selectivity. In this contribution, we use silica-supported cobalt catalysts as a case study, elucidate the cause for nanoparticle aggregation by an extensive study of the drying step, show how to control the extent of aggregation, and report the effect on Fischer−Tropsch catalysis.

EXPERIMENTAL SECTION

Co/SiO_2 catalysts were prepared using a commercially available silica gel as support (Davicat 1404, Grace-Davidson). The support grains were sieved to a fraction of 38−75 μm, and the porosity was characterized with N_2-physisorption at −196 °C (Tristar 3000, Micromeritics): V_p = 0.87 cm^3/g, S_{BET} = 443 m^2/g, d_p = 8 nm. Solution impregnation was performed to incipient wetness using a 4.2 M $Co(NO_3)_2{\cdot}6H_2O$ (Sigma-Aldrich, >99%) (aq) solution leading to a nominal cobalt metal loading of 16.2 wt %. Pt-promoted samples were impregnated with a 4.2 M $Co(NO_3)_2{\cdot}6H_2O$, 0.03 M $(NH_3)_4Pt(NO_3)_2$ (Alfa Aesar, 99.99%) (aq) solution to obtain 0.5 wt % Pt and 16.2 wt % Co.

Different drying treatments were applied by transferring 100 or 400 mg of the impregnated grains into an upflow fluidized bed reactor (internal diameter of 1 or 2 cm, respectively). After the oven reached the drying temperature, the reactor was placed in the oven, and an N_2 flow with a gas hourly space velocity (GHSV) of 5000 h^{-1} was applied. Catalysts were dried at 25, 50, 75, 100, 125, and 150 °C for 48, 24, 16, 3, 3, and 2 h, respectively. Calcination of all dried catalysts was performed by further heating the fluidized bed reactor to 350 °C (1 °C/min, 1h) in a flow of N_2 (GHSV 30000 h^{-1}).

The phase behavior of cobalt nitrate present during the different stages of catalyst preparation was analyzed using differential scanning calorimetry (DSC, Q2000, TA Instruments). The temperature and heat flow were calibrated with a certified indium sample, and measurements were performed with hermetically sealed aluminum pans (~40 μL, Tzero, TA Instruments) under a flow of N_2 (50 mL/min). Sample masses were typically between 5 and 15 mg, and heat flows were recorded between −90 and 120 °C at a rate of 1 °C/min.

Thermogravimetric analysis (TGA, Q50 TA Instruments) was used to determine the residual water content after different drying treatments by measuring the weight loss after heating to 500 °C for 30 min (10 °C/min) under a 60 mL/min N_2 flow. The weight loss was corrected for the loss of water by condensation of silanol groups from the pristine silica gel, which was experimentally found to occur between 150 and 500 °C. The rest of the weight loss was attributed to residual water or the decomposition of $Co(NO_3)_2$ to Co_3O_4 after drying at 125 and 150 °C, as was evident from the black color of the samples.

The degree of reduction was measured using TGA (Pyris 1 TGA, PerkinElmer) in a flow of 10% H_2/He. Ten mg of sample was heated at 2 °C/min to 350 or 500 °C for the Pt promoted and unpromoted samples, respectively, and held there for 3 h. While this was shorter compared to the reduction prior to catalysis experiments, no significant weight loss was observed after this time.

H_2-chemisorption measurements were performed on a Micromeretics ASAP 2020 instrument. Samples were dried at 100 °C for 1 h in dynamic vacuum followed by a reduction in H_2 at 350 or 500 °C (5 h, 2 °C/min). Isotherms were measured at 150 °C. Apparent cobalt surface areas were calculated assuming H:Co = 1 and an atomic cross-section of 0.0662 nm^2. The corrected particle sizes were deduced from the cobalt surface areas using the amount cobalt per gram of catalysts multiplied by the degree of reduction.

XRD patterns were recorded between 20 and 90° 2θ with a Bruker-AXS D2 Phaser X-ray Diffractometer using Co-$K_{\alpha 12}$ radiation (λ = 1.790 Å). The volume averaged Co_3O_4 crystallite size was determined using the Scherrer equation with a shape factor k = 0.9 and line broadening analysis on the (110), (111), and (200) peaks by a fitting procedure in Eva2 software (Bruker AXS).

N_2-physisorption isotherms were measured at −196 °C using a Micromeritics Tristar 3000 apparatus. Prior to analysis, samples were dried in He flow for 16 h at 200 °C. For the spent catalysts, several samples were measured before and after heat treatment in a muffle oven at 500 °C in air to remove all the waxes present in the pores.

Catalyst grains were embedded in a two component epoxy resin (Epofix, EMS) and cured at 60 °C overnight. The embedded catalysts were then cut into thin sections with a nominal thickness of 50 nm using a Diatome Ultra 35° diamond knife mounted on a Ultracut E microtome (Reichert-Jung) and collected on a TEM grid. Bright-field TEM images were obtained on a Tecnai 12 (FEI), operated at 120 keV.

Dark-field images were taken to study the crystallinity of the aggregates at 80 keV by tilting the incoming electron beam 1.2°. The smallest objective aperture was used so that only diffracted electrons in a small rotational range were selected, allowing for the imaging of crystallites which were crystallographically aligned. The incoming electron beam was then rotated 10° for each subsequent image so that a semicircle of 180° was measured.

EDX analysis was used to measure the cobalt weight loading of the spent catalysts in a Technai 20-FEG (FEI) electron microscope operating at 200 keV. For each sample, EDX was performed on large areas (>100 μm^2) of the microtomed sections of 5−10 catalyst grains to measure the average Co/Si atomic ratio of the grains.

Low-resolution SEM was performed on a PHENOM SEM (Phenom World) equipped with a backscatter detector operated at 5 keV. For high resolution SEM, samples were coated with a thin layer of Pt, after which the measurements were performed on a XL30SFEG (FEI).

Catalysis was performed on a Flowrence (Avantium) 16 parallel reactor unit. 50 or 70 mg of the Pt-promoted or unpromoted catalyst (38−75 μm), respectively, was mixed with 200 mg SiC (100−200 μm) and loaded into a stainless steel reactor. Catalysts were reduced in situ in 25 vol % H_2/He by going to 350 or 500 °C, respectively, at 1 °C/min and held for 8 h. Afterward, the reactors were cooled to 180 °C at which the pressure was increased to 20 bar under H_2. Next, the feed was changed to an H_2/CO ratio of 2.0 with 5 vol % He, which functioned as internal standard for the online GC (Agilent 7890A). After 1 h, the temperature was increased to the reaction temperature of 220 °C at 1 °C/min. All catalysts started at a CO conversion around 80%. After 240 h on-stream at high CO conversion levels, the catalysts were flushed with argon, and subsequently the reactors were repressurized to 20 bar under H_2 at 180 °C, after which syngas was reintroduced and the temperature was returned to 220 °C. Next, the conversion was lowered by increasing the GHSV, to measure the selectivity of all catalysts at a CO conversion of 65% after 10 h. The C_{5+} selectivity was calculated by subtracting the amount of CO used for the formation of C_1 to C_4 products, as determined via online GC using He as an internal standard, from the total amount of CO converted.

RESULTS AND DISCUSSION

Co/SiO_2 catalysts with a 16 wt % Co loading were synthesized by incipient wetness impregnation of silica gel grains with a saturated $Co(NO_3)_2{\cdot}6H_2O$ solution. Subsequently, N_2 fluidized bed drying treatments were applied at six different temperatures to different batches of the impregnated catalysts, followed by calcination at 350 °C in N_2 flow. Table 1 shows the Co_3O_4 crystallite size after drying and calcination obtained from XRD, averaging around 8.5 nm regardless of the drying treatment. This is close to the average pore diameter of the support and suggests particles grew in confinement of the pores, as has been reported before.[41]

Figure 1 shows TEM micrographs of the same catalysts. Drying at 25 °C resulted in cobalt aggregates with an average size of 25 nm. These aggregates became smaller as the drying

dx.doi.org/10.1021/ja500436y | J. Am. Chem. Soc. 2014, 136, 7333−7340

Table 1. Precursor Properties Obtained after Drying and after Calcination of the Cobalt Nitrate Impregnated Silica Grains

drying temperature (°C)	H_2O content after drying (mol_{H_2O}/mol_{Co})[a]	$Co(NO_3)_2$ converted to Co_3O_4 during drying[a]	Co_3O_4 crystallite size (XRD) after calcination (nm)	aggregate size (TEM) after calcination (nm)
25	4.5	0%	8.7	25 (±6)
50	1.4	0%	8.5	18 (±4)
75	0.6	0%	7.8	14 (±2)
100	0.4	0%	8.5	11 (±2)
125	0	17%	8.7	26 (±6)
150	0	55%	9.4	44 (±10)

[a]Determined by TGA after drying.

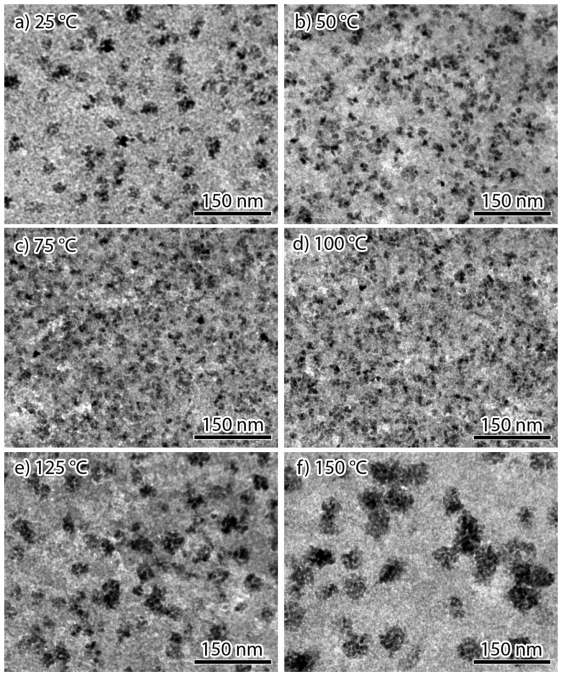

Figure 1. TEM of calcined Co_3O_4/SiO_2 after different drying treatments, showing different aggregate sizes (black) on the silica support (gray) depending on the drying temperature. Dried at (a) 25 °C, (b) 50 °C, (c) 75 °C, (d) 100 °C, (e) 125 °C, and (f) 150 °C.

temperature increased, until at 100 °C most of the crystallites were isolated instead of aggregated. Further increase in temperature resulted in an increase in aggregate size, as large as 50 nm after drying at 150 °C.

Figure 2 shows dark-field (DFTEM) analysis of the catalyst dried at 150 °C and subsequently calcined, which allows imaging of electrons diffracted by only a specific Co_3O_4 lattice plane depending on the orientation of the crystallite. Many aggregates were observed as a single color or not at all, suggesting they consisted of a single crystalline domain of multiple nanocrystals. These crystalline domains likely grew around the support grains, as has previously been observed for cobalt on γ-alumina,[39,42] and which was confirmed by removing the silica, leaving aggregated cobalt particles with the size of the aggregates with well-defined pores (see Figure S5).

TGA was performed to study the water content of the catalyst precursor after drying (Table 1). After drying at 25 °C, 4 mol H_2O/mol Co remained. Higher drying temperatures

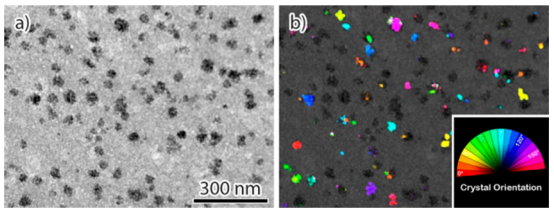

Figure 2. DFTEM of Co_3O_4/SiO_2 synthesized by drying at 150 °C, followed by calcination. (a) Bright-field image, showing large cobalt oxide aggregates (black). (b) Superposition of 18 dark-field images separated by a beam orientation of 10° each. Crystal lattice orientation of the aggregates is represented by different colors (inset).

resulted in less residual water, and at 100 °C the sample was almost completely dehydrated. Temperatures above 100 °C resulted in partial conversion of cobalt nitrate into cobalt oxide during drying. At 150 °C, 55% of the cobalt nitrate was decomposed during the drying treatment. Phase analysis was performed for each sample after drying by DSC, however no melting peaks were observed between −90 and +120 °C for any of the samples, suggesting the remaining precursor had precipitated as solid cobalt nitrate or cobalt oxide species. These results, along with samples obtained by varying the drying time and gas hourly space velocity and the subsequent temperature ramp during calcination (see Figures S1−S3) allowed us to tentatively propose two different mechanisms for the formation of cobalt oxide aggregates.

At temperatures below 100 °C aggregation is attributed to the slow drying process. At a certain point during drying, the water content becomes so low that a solid cobalt nitrate phase precipitates. When such a transition is slow, severe redistribution of remaining liquid may take place on a nanoscale, as is well-known for the drying of colloidal films.[43] Nucleation of the precipitated phase combined with extensive growth could result in the formation of cobalt nitrate rich and poor areas, the sizes of which depend on the mobility of the precursor while still in solution and the allowed time for redistribution. These cobalt nitrate-rich areas are then the basis to form Co_3O_4 aggregates upon further heat treatment. Thus, at 25 °C, when drying takes long and the transition is presumed to be slow, aggregation was observed, whereas increasing the temperature to 100 °C gradually reduced the aggregation. Macroscopically, the drying rate was recently shown to influence the distribution of low melting point metal nitrates at high concentration.[44] However, by utilizing ultramicrotomy, the distribution for each catalyst was verified to be uniform throughout the 38−75 μm catalyst grains, suggesting our system was not sensitive to macroscopic redistribution effects under the used conditions.

The most uniform distribution at the nanoscale obtained after drying at 100 °C is explained from fast drying that restricts redistribution of viscous liquids.[44] Above 100 °C, nucleation and growth of Co_3O_4 from cobalt nitrate becomes possible. This already occurs before the sample is completely dried, while cobalt nitrate has not yet precipitated and due to reduced viscosity has high mobility. Indeed, a high water partial pressure during high temperature drying, or insufficient removal of water during calcination, is known to result in severe agglomeration.[45−47] We postulate that this interplay between temperature, viscosity, and water partial pressure leads to the formation of the observed aggregates, whereby growth from capturing cobalt from solution is favorable over nucleation of Co_3O_4, leading to large aggregates of crystallographically

dx.doi.org/10.1021/ja500436y | J. Am. Chem. Soc. 2014, 136, 7333−7340

Table 2. Catalyst Aggregate Size, Properties after Reduction and Catalytic Activity, Selectivity, and Deactivation Rate Constant Obtained After 240 h on Stream at 20 bar, 220 °C, H_2/CO 2.0[a]

catalyst	aggregate size (nm)	Co surface area (m^2/g_{Co})	degree of reduction (%)	corrected Co particle size (nm)	TOF (10^{-2} s^{-1})	CTY (10^{-5} $mol_{CO}g_{Co}^{-1}$ s^{-1})	C_1 (wt %)	C_{5+} (wt %)	$k_{D,2}$ (10^{-4} h^{-1})[b]
CoD100	13 (±3)	57	78%	9.2	4.6	6.5	8.6	83.3	14.7
CoD125	22 (±6)	55	76%	9.3	4.1	5.8	8.5	83.5	16.0
CoD150	37 (±9)	55	83%	10.1	4.4	5.6	8.5	84.1	17.3
CoD175	77 (±18)	55	84%	10.3	3.9	5.3	8.4	84.5	19.3
CoPtD100	11 (±4)	80	105%	8.4	3.9	7.9	9.5	82.9	5.3
CoPtD125	18 (±5)	74	103%	9.1	4.5	8.2	8.9	83.6	9.4
CoPtD150	38 (±10)	85	96%	8.0	4.3	8.9	8.6	83.6	11.0
CoPtD175	74 (±18)	75	93%	8.3	4.3	8.2	7.9	85.0	13.6

[a]Activity and selectivity reported at 65% CO conversion. [b]Deactivation rate constant was defined as $a_{norm}^{1-n} = (n-1)\cdot k_D \cdot t + 1$, whereby a_{norm} is a measure for the normalized activity assuming first-order kinetics so that $a = -\ln(1 - \text{conversion}_{CO})$ and $n = 2$ (see Supporting Information)

aligned cobalt oxide particles which originate from a single nucleation point.[48]

To study the effect of aggregation on Fischer–Tropsch catalysis, catalysts with four aggregate sizes between 10 and 80 nm were synthesized using four drying temperatures between 100 and 175 °C, indicated after the D in the sample name. In one set of catalysts, 0.5 wt % Pt was added as a reduction promoter.[49] Table 2 shows the average aggregate size of each catalyst as determined by TEM as well as the Co surface area, degree of reduction, and corrected cobalt metal particle size.

To ensure a high degree of reduction, the unpromoted catalysts were reduced at 500 °C, while the Pt promoted catalysts were reduced at 350 °C. This resulted in an average degree of reduction of 80% and average cobalt surface area of 55 m^2/g_{Co} for the unpromoted catalysts, while the promoted catalysts showed almost complete reduction and averaged around 80 m^2/g_{Co} regardless of aggregate size. Consequently, the particle sizes of all catalysts were similar, between 8 and 10 nm, close to the support pore diameter (Table 2).

TEM on reduced and passivated CoPt catalysts (Figure S4) showed that the aggregates were still present, but now also distinct Co particles within the aggregates were observed. DFTEM (Figure 3) showed many particles in a single aggregate

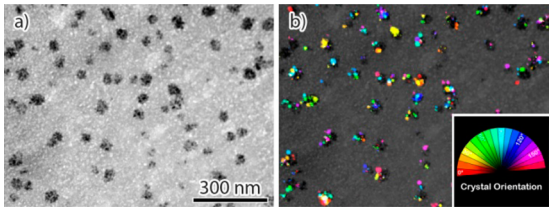

Figure 3. DFTEM of CoPtD150 after reduction and passivation. (a) Bright-field image, showing large cobalt aggregates. (b) Superposition of 18 dark-field images separated by a beam orientation of 10° each. Crystal lattice orientation of the individual nanoparticles is represented by different colors (inset).

to have different crystal orientations. This indicated that after reduction the aggregates had broken up into smaller nonaligned crystallites, similar to what was previously reported for large cobalt oxide particles in model systems.[50,51] Thus, during the initial stages of catalysis the aggregates consisted of many individual particles with very small but finite interparticle distances.

The catalysts were tested at 220 °C, 20 bar, and a H_2/CO ratio of 2.0. Table 2 shows the catalytic data after 240 h on-stream. An average TOF of 4.2×10^{-2} s^{-1} was found with no significant difference between the promoted and unpromoted samples, as expected for cobalt particles larger than 6 nm.[52] Consequently, the promoted catalysts were 40% more active on average (CTY, see Table 2), due to their slightly smaller cobalt particles and higher degree of reduction. Little effect of aggregation on activity was found. Only for the unpromoted catalysts an effect of the aggregate size was observed, the most uniformly distributed catalyst being 25% more active compared to the highly aggregated catalyst. Also an increasing C_{5+} selectivity for increasing aggregate size was apparent, accompanied by a decrease in the methane selectivity (Table 2). An increase in olefin production was also observed for catalysts with larger aggregates (see Figure S8a). This suggests that enhanced formation, readsorption, and secondary chain growth of olefins inside aggregates is the cause of the increased selectivity. The olefin production for all Pt promoted catalysts was lower than for the corresponding unpromoted catalysts, attributed to the additional hydrogenation activity of the platinum.

All catalysts were observed to deactivate (Figure S7a) and second-order deactivation rate constants, which are a measure of the decrease in activity per hour (see Supporting Information), are shown in Table 2 and Figure 4. CoPtD100 exhibited the lowest deactivation rate constant of 5.3×10^{-4} h^{-1}, which increased up to 13.6×10^{-4} h^{-1} for CoPtD175. All unpromoted catalysts had higher deactivation constants, ranging from 14.7 to 19.3 $\times 10^{-4}$ h^{-1} for CoD100 and

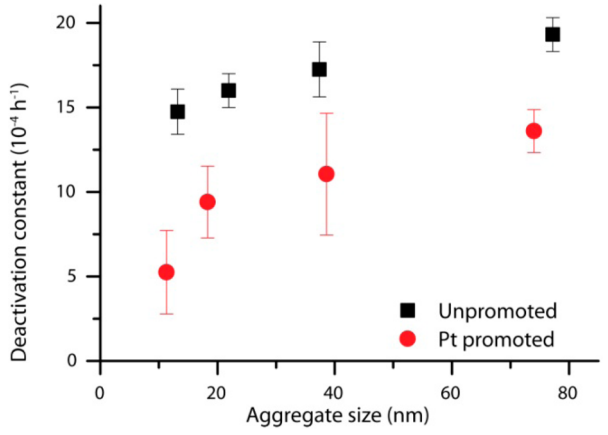

Figure 4. Deactivation rate constants measured during 240 h of Fischer–Tropsch activity as a function of the cobalt aggregate size in Co/SiO_2 (black) and $Co/Pt/SiO_2$ (red) catalysts.

dx.doi.org/10.1021/ja500436y | J. Am. Chem. Soc. 2014, 136, 7333–7340

CoD175, respectively. Thus, two effects were found to influence the stability of the catalysts. First, introducing Pt lowered the deactivation rate for each catalyst, and catalysts containing larger aggregates of cobalt particles were found to deactivate faster.

Deactivation in Fischer–Tropsch catalysts can occur via several different pathways, such as poisoning, carbon deposition, and particle growth, often occurring simultaneously to some degree.[30] In addition, a high steam pressure, such as found at the bottom of the reactor, could affect the SiO_2 support. N_2 physisorption experiments (see Table S1) excluded the latter as significant for the conditions and time frame studied, and no evidence of large amounts of cobalt silicates was found in TEM micrographs of spent catalysts.[53] Carbon deposition has previously been reported to cause long-term deactivation and is difficult to avoid.[54] Noble metal promoters can prevent extensive formation of polymeric carbon,[55−57] which could explain the difference in deactivation between unpromoted and Pt promoted catalysts observed in Figure 4. The particles within aggregates have very short interparticle distances, so that particle growth likely contributed to deactivation.

Figure 5 shows TEM images of CoPtD100 and CoD175 after reduction and after catalysis from the top half and bottom half

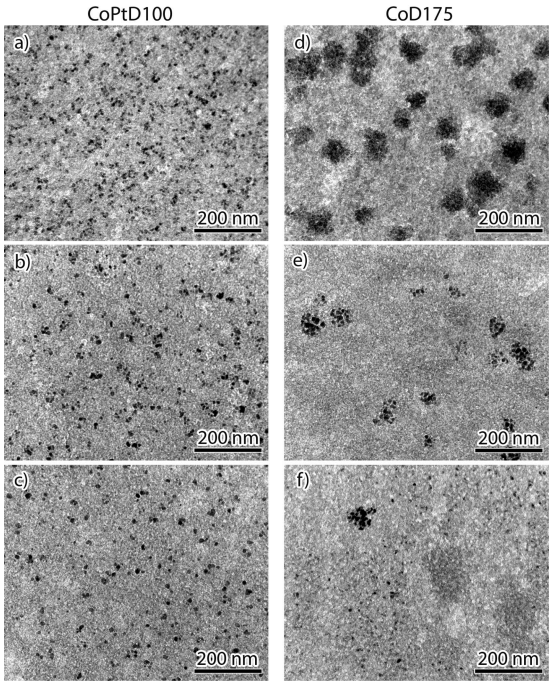

Figure 5. TEM comparison of fresh and spent Co/SiO_2 catalysts. (a) CoPtD100 after reduction, (b) CoPtD100 after reaction from the top half, and (c) CoPtD100 from the bottom half of the reactor. (d) CoD175 after reduction, (e) CoD175 after reaction from the top half, and (f) CoD175 after reaction from the bottom half of the reactor.

of the reactor, respectively. Aggregates of cobalt nanoparticles were found to have fragmented into more isolated nanoparticles upon catalysis, as shown, for example, by comparison of Figure 5d with 5e,f. This breakup of aggregates was more apparent for larger aggregates and had occurred more extensively in the bottom of the reactor where the CO conversion was highest (see also Figure S12). Surprisingly, the cobalt particles did not exhibit a significant increase in size, as shown by TEM histogram analysis (see Table S2). However, although no increase in cobalt particle size was observed after catalysis, a decrease in particle density on the support is apparent from Figure 5. EDX analysis of the Co/Si atomic ratio of the microtomed sections of the spent catalysts was used to investigate this apparent cobalt mass loss. Fresh catalysts showed to have a weight loading of 16.2 wt %, whereas all spent catalysts contained less cobalt. A correlation was found between the loss of cobalt inside of the catalyst grains and the loss in activity (Figure 6); the higher the loss in cobalt, the higher the

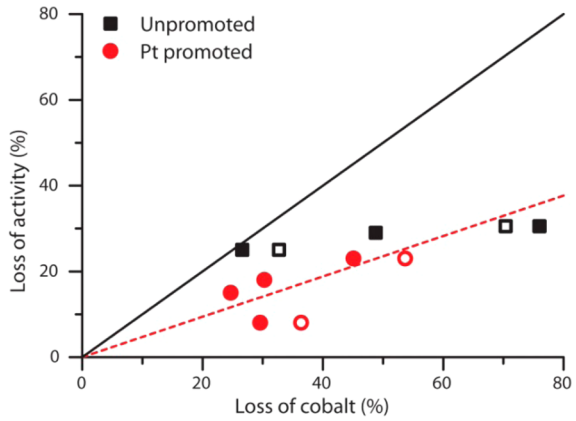

Figure 6. Loss of cobalt (from EDX) inside promoted and unpromoted Co/SiO_2 catalyst grains after catalysis taken from the top half (open symbol) or bottom half (closed symbol) of the reactor, related to the loss in activity of the corresponding catalyst assuming first-order kinetics. The black line illustrates the expected activity loss if the cobalt was lost from the reactor or sintered into very large particles.

loss in activity. The cobalt loading inside the catalyst grains could be as low as 4 wt % for CoD175 after catalysis, 75% less than the nominal loading. However, the activity decreased only by about 30%, less than half of what was expected given the observed loss in cobalt and the similar particle size. Clearly, the question comes up: What is the fate of the cobalt that is lost from the interior of the catalyst grains?

SEM images of macroscopic catalyst grains before and after catalysis are shown in Figure 7a,b. Before catalysis, no cobalt was observed on the external surface of CoD175 (Figure 7a). However, after reaction large cobalt-rich areas were found on the exterior surfaces of catalyst grains (Figure 7b). This was observed for each catalyst, whereby the largest amount of cobalt was observed on the exterior surface of catalysts originally with the largest aggregates, such as CoD175 and CoPtD175, while CoD100 and CoPtD100, the catalysts with homogeneously distributed nanoparticles, had much less cobalt on the outer surface (see Figure S15). Thus, it was concluded that the difference in deactivation between homogeneously distributed and aggregated catalysts coincided with the migration of cobalt over macroscopic distances to the outside of the catalyst grains.

HAADF-STEM tomography revealed that aggregates on the external surface of the grains consisted of large solid particles of ~300 nm in size on top of small particles (Figure 7c,d,e). See Supporting Information for movies of the full tomogram and tilt series. Histogram analysis on the small particles showed the average particle size within these aggregates was 9.7 nm (±2.2), identical to the size of the fresh and spent catalysts (Figure S14). Thus, the cobalt that migrated to the external surface was

dx.doi.org/10.1021/ja500436y | J. Am. Chem. Soc. 2014, 136, 7333−7340

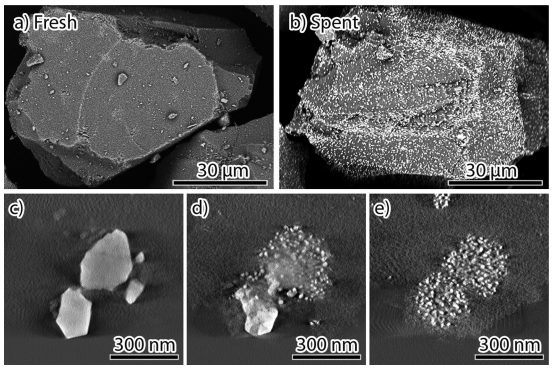

Figure 7. (a,b) SEM comparison of the external surface of Co/SiO_2 grains from CoD175 after (a) reduction and (b) catalysis. Before catalysis, little cobalt was observed on the external surface of the grains, whereas after catalysis a huge amount of cobalt was observed indicated by the bright spots. (c,d,e) Slices from an HAADF-STEM tomography reconstruction of an aggregate at the external surface of a grain of the spent CoD175, separated by 75 nm in the z direction, illustrating the aggregate consisted of large solid cobalt particles of 100−300 nm (c), on top of many smaller cobalt particles of about 10 nm (d,e).

deposited as many small particles that still contributed to the catalytic activity, however sintering also occurred on the external surface, forming huge particles. This explains the difference between the observed loss of cobalt and loss of activity in Figure 6.

Migration of cobalt over macroscopic distances has been previously observed on γ-Al_2O_3 by Khodakov et al. and attributed to high temperature effects or low H_2/CO ratios and low gas flow rates.[58,59] However, here we show for the first time that the degree of redistribution on the macroscale was greatly influenced by the nanoscale cobalt distribution. The exact mechanism for this long-range migration is as yet unknown. Because the cobalt particles found inside the catalyst grains and those that migrated toward external surface were similar in size, Ostwald ripening is an unlikely candidate, since this concerns transport from small to larger particles. Partial oxidation during Fischer−Tropsch conditions and migration of entire particles has been proposed as a mechanism for sintering by Khodakov et al.,[60] and evidence for (surface) oxidation of cobalt particles has been observed in some studies.[61−63] Catalysts with a low deactivation rate exhibited a relatively high hydrogenation activity, as observed from the propene/propane ratio, which could support this mechanism (see Figure S8). However, calculations based on literature data[60,64,65] suggest classical random-walk diffusion of (oxidized) Co particles over the surface of the support can be excluded for transport over macroscopic distances. The diffusion coefficient of nanoparticles in a colloidal state is orders of magnitude higher, so that diffusion of the particles in liquid phase is a possible transport mechanism. Moreover, because particles are collected in aggregates at the external surface we tentatively propose entrainment of particles by reaction products to be responsible for the observed migration. At high conversion, confinement in the small silica pores and the presence of a hydrophobic liquid phase of long-chain alkanes could lead water vapor to condense into small droplets. Droplets expelled to the outside surface of the catalyst particle by the formation of new reaction products will transport the cobalt particles in the liquid phase by entrainment. If the water droplets evaporate on the outside of the catalyst grains once no longer confined, deposition of the entrained cobalt particles at the external surface takes place.

CONCLUSION

Aggregation of supported metal nanoparticles during the synthesis of ex-nitrate catalysts was strongly affected by the drying step after impregnation of a silica support with a metal nitrate precursor solution. At low temperatures, aggregation occurred as dissolved metal nitrate species were given ample time to redistribute before and during precipitation of the solid phase. At high temperatures, aggregation was caused by decomposition of the metal nitrate into the metal oxide during the drying process, which was aggravated by the mobile precursor at high water vapor pressures. At intermediate temperature (100 °C), aggregation could be largely prevented, and by utilization of a fluid bed drying process isolated nanoparticles on the support were obtained.

After calcination, the aggregates consisted mainly of crystallographically aligned nanoparticles throughout the porous network. During reduction these aggregated crystallites fragmented into smaller particles with small interparticle spacing. Large aggregates of cobalt nanoparticles exhibited somewhat higher C_{5+} selectivities in Fischer−Tropsch catalysis, attributed to higher olefin formation, readsorption, and consecutive chain growth. A difference in deactivation between unpromoted and platinum promoted catalysts could indicate carbon deposition as a relevant deactivation mehanism. Moreover, an additional form of deactivation occurred not via direct nanoparticle growth but via the migration over macroscopic distances of cobalt nanoparticles to the external surface of the catalyst grains. Only once on the surface of the catalyst grains, particles could sinter together into very large cobalt particles. This migration likely resulted from nanoparticles being entrained over distances of many micrometers from their original location and was found to be more extensive for large initial aggregate sizes. By creating more uniformly dispersed catalysts, the degree of migration to the external surface of the catalyst grains was greatly reduced. These results are not only highly important for the rational design of supported cobalt catalysts but point to the general relevance of nanoparticles distribution and spacing as an important design criterion of functional nanomaterials.[66−69]

ASSOCIATED CONTENT

Supporting Information

Experimental details, including synthesis, characterization, and catalysis. Additional characterization data, including additional TEM, investigation of aggregates, catalytic data, and method for determinging the deactivation, and additional characterization on spent catalysts. Two videos showing the tilt series and tomography reconstruction of a spent catalyst. This material is available free of charge via the Internet at http://pubs.acs.org/

AUTHOR INFORMATION

Corresponding Author

k.p.dejong@uu.nl

Notes

The authors declare no competing financial interest.

ACKNOWLEDGMENTS

The Netherlands Organization for Scientific Research is acknowledged for funding (NWO TOP 700.57.341). Mr. M.

van Steenbergen and Dr. H. Talsma (Utrecht University) are acknowledged for their help with the DSC and TGA measurements on dried samples. Mr. H. Meeldijk (Utrecht University) is acknowledged for EDX analysis and tomography. Ms. M. Versluis-Helder (Utrecht University) is acknowledged for the TGA-reduction measurements and high-resolution SEM. Ms. E. van Donselaar (Utrecht University) is acknowledged for ultramicrotomy instructions. Mr. J. H. den Otter (Utrecht University) is acknowledged for H_2-chemisorption and N_2-physisorption measurements.

REFERENCES

(1) Galeano, C.; Meier, J. C.; Peinecke, V.; Bongard, H.; Katsounaros, I.; Topalov, A. a; Lu, A.; Mayrhofer, K. J. J.; Schüth, F. *J. Am. Chem. Soc.* **2012**, *134*, 20457.
(2) Torres Galvis, H. M.; Bitter, J. H.; Khare, C. B.; Ruitenbeek, M.; Dugulan, A. I.; de Jong, K. P. *Science* **2012**, *335*, 835.
(3) Bezemer, G. L.; Bitter, J. H.; Kuipers, H. P. C. E.; Oosterbeek, H.; Holewijn, J. E.; Xu, X. D.; Kapteijn, F.; van Dillen, J. A.; de Jong, K. P. *J. Am. Chem. Soc.* **2006**, *128*, 3956.
(4) Wynblatt, P.; Gjostein, N. A. *Prog. Solid State Chem.* **1975**, 21.
(5) Ouyang, R.; Liu, J.-X.; Li, W.-X. *J. Am. Chem. Soc.* **2013**, *135*, 1760.
(6) Parkinson, G. S.; Novotny, Z.; Argentero, G.; Schmid, M.; Pavelec, J.; Kosak, R.; Blaha, P.; Diebold, U. *Nat. Mater.* **2013**, *12*, 724.
(7) Hansen, T. W.; Delariva, A. T.; Challa, S. R.; Datye, A. K. *Acc. Chem. Res.* **2013**, *46*, 1720.
(8) Campbell, C. T.; Parker, S.; Starr, D. *Science* **2002**, *298*, 811.
(9) Cao, A.; Veser, G. *Nat. Mater.* **2010**, *9*, 75.
(10) Farmer, J. A.; Campbell, C. T. *Science* **2010**, *329*, 933.
(11) Soled, S. L. *Synthesis of Solid Catalysts*; de Jong, K. P., Ed.; WILEY-VCH Verlag GmbH& Co. KGaA: Weinheim, 2009.
(12) Prieto, G.; Zečević, J.; Friedrich, H.; de Jong, K. P.; de Jongh, P. E. *Nat. Mater.* **2013**, *12*, 34.
(13) Friedrich, H.; Sietsma, J. R. A.; de Jongh, P. E.; Verkleij, A. J.; de Jong, K. P. *J. Am. Chem. Soc.* **2007**, *129*, 10249.
(14) Jiao, L.; Regalbuto, J. R. *J. Catal.* **2008**, *260*, 342.
(15) Den Breejen, J. P.; Frey, A. M.; Yang, J.; Holmen, A.; Schooneveld, M. M.; Groot, F. M. F.; Stephan, O.; Bitter, J. H.; de Jong, K. P. *Top. Catal.* **2011**, *54*, 768.
(16) Bae, J. W.; Kim, S.-M.; Kang, S.-H.; Chary, K. V. R.; Lee, Y.-J.; Kim, H.-J.; Jun, K.-W. *J. Mol. Catal. A Chem.* **2009**, *311*, 7.
(17) Girardon, J. S.; Lermontov, A. S.; Gengembre, L.; Chernavskii, P. A. *J. Catal.* **2005**, *230*, 339.
(18) Panpranot, J.; Kaewkun, S.; Praserthdam, P.; Goodwin, J. G. *Catal. Lett.* **2003**, *91*, 95.
(19) Rane, S.; Borg, Ø.; Rytter, E.; Holmen, A. *Appl. Catal. A Gen.* **2012**, *437*−*438*, 10.
(20) Borg, Ø.; Dietzel, P. D. C.; Spjelkavik, A. I.; Tveten, E. Z.; Walmsley, J. C.; Diplas, S.; Eri, S.; Holmen, A.; Rytter, E. *J. Catal.* **2008**, *259*, 161.
(21) Hong, J.; Marceau, E.; Khodakov, A. Y.; Griboval-Constant, A.; La, C.; Briois, V.; Chernavskii, P. A. *Catal. Today* **2011**, *175*, 528.
(22) Dumond, F.; Marceau, E.; Che, M. *J. Phys. Chem. C* **2007**, *111*, 4780.
(23) Zhang, Y.; Liu, Y.; Yang, G.; Sun, S.; Tsubaki, N. *Appl. Catal. A Gen.* **2007**, *321*, 79.
(24) Kok, E.; Cant, N.; Trimm, D.; Scott, J. *Catal. Today* **2011**, *178*, 79.
(25) Neimark, A. V.; Kheifez, L. I.; Fenelonov, V. B. *Ind. Eng. Chem. Prod. Res. Dev.* **1981**, 439.
(26) Lekhal, A.; Glasser, B. J.; Khinast, J. G. *Chem. Eng. Sci.* **2001**, *56*, 4473.
(27) Bogdanchikova, N. E.; Tretyakov, V. V. *Preparation of Catalysts V*; Poncelet, G., Jacobs, P. A., Grange, P., Delmon, B., Eds.; Elsevier: Amsterdam, 1991; pp 647−652.
(28) Eggenhuisen, T. M.; Friedrich, H.; Nudelman, F.; Zečević, J.; Sommerdijk, N. A. J. M.; de Jongh, P. E.; de Jong, K. P. *Chem. Mater.* **2013**, *25*, 890.
(29) Eggenhuisen, T. M.; Munnik, P.; Talsma, H.; de Jongh, P. E.; de Jong, K. P. *J. Catal.* **2013**, *297*, 306.
(30) Tsakoumis, N. E.; Rønning, M.; Borg, Ø.; Rytter, E.; Holmen, A. *Catal. Today* **2010**, *154*, 162.
(31) Saib, A. M.; Moodley, D. J.; Ciobîc, I. M.; Hauman, M. M.; Sigwebela, B. H.; Weststrate, C. J.; Niemantsverdriet, J. W.; van de Loosdrecht, J. *Catal. Today* **2010**, *154*, 271.
(32) Karaca, H.; Safonova, O. V.; Chambrey, S.; Fongarland, P.; Roussel, P.; Griboval-Constant, A.; Lacroix, M.; Khodakov, A. Y. *J. Catal.* **2011**, *277*, 14.
(33) Karaca, H.; Hong, J.; Fongarland, P.; Roussel, P.; Griboval-Constant, A.; Lacroix, M.; Hortmann, K.; Safonova, O. V.; Khodakov, A. Y. *Chem. Commun.* **2010**, *46*, 788.
(34) Das, T. K.; Jacobs, G.; Davis, B. H. *Catal. Lett.* **2005**, *101*, 187.
(35) Bezemer, G. L.; Remans, T. J.; van Bavel, A. P.; Dugulan, A. I. *J. Am. Chem. Soc.* **2010**, *132*, 8540.
(36) Borg, Ø.; Eri, S.; Blekkan, E. A.; Storsæter, S.; Wigum, H.; Rytter, E.; Holmen, A. *J. Catal.* **2007**, *248*, 89.
(37) Roy, M.; Marion, M. U.S. Patent: 6235798B1, 2001.
(38) Saib, A. M.; Claeys, M.; van Steen, E. *Catal. Today* **2002**, *71*, 395.
(39) Borg, Ø.; Walmsley, J. C.; Dehghan, R.; Tanem, B. S.; Blekkan, E. A.; Eri, S.; Rytter, E.; Holmen, A. *Catal. Lett.* **2008**, *126*, 224.
(40) Feller, A.; Claeys, M.; van Steen, E. *J. Catal.* **1999**, *185*, 120.
(41) Wolters, M.; van Grotel, L. J. W.; Eggenhuisen, T. M.; Sietsma, J. R. A.; de Jong, K. P.; de Jongh, P. E. *Catal. Today* **2011**, *163*, 27.
(42) Arslan, I.; Walmsley, J. C.; Rytter, E.; Bergene, E.; Midgley, P. A. *J. Am. Chem. Soc.* **2008**, *130*, 5716.
(43) Vancea, I.; Thiele, U.; Pauliac-Vaujour, E.; Stannard, A.; Martin, C. P.; Blunt, M.; Moriarty, P. *Phys. Rev. E* **2008**, *78*, 1.
(44) Liu, X.; Khinast, J. G.; Glasser, B. J. *Chem. Eng. Sci.* **2012**, *79*, 187.
(45) Sun, X.; Shi, Y.; Zhang, P.; Zheng, C.; Zheng, X.; Zhang, F.; Zhang, Y.; Guan, N.; Zhao, D.; Stucky, G. D. *J. Am. Chem. Soc.* **2011**, *133*, 14542.
(46) Sietsma, J. R. A.; Meeldijk, J. D.; den Breejen, J. P.; Versluijs-Helder, M.; van Dillen, J. A.; de Jongh, P. E.; de Jong, K. P. *Angew. Chem., Int. Ed.* **2007**, *46*, 4547.
(47) Wolters, M.; Munnik, P.; Bitter, J. H.; de Jongh, P. E.; de Jong, K. P. *J. Phys. Chem. C* **2011**, 3332.
(48) Castner, D. G.; Watson, P. R.; Chan, I. Y. *J. Phys. Chem.* **1989**, *93*, 3188.
(49) Jacobs, G.; Das, T. K.; Zhang, Y.; Li, J.; Racoillet, G.; Davis, B. H. *Appl. Catal. A Gen.* **2002**, *233*, 263.
(50) Weststrate, C. J.; Hauman, M. M.; Moodley, D. J.; Saib, A. M.; van Steen, E.; Niemantsverdriet, J. W. *Top. Catal.* **2011**, 811.
(51) Dehghan, R.; Hansen, T. W.; Wagner, J. B.; Holmen, A.; Rytter, E.; Borg, Ø.; Walmsley, J. C. *Catal. Lett.* **2011**, *141*, 754.
(52) Den Breejen, J. P.; Radstake, P. B.; Bezemer, G. L.; Bitter, J. H.; Frøseth, V.; Holmen, A.; de Jong, K. P. *J. Am. Chem. Soc.* **2009**, *131*, 7197.
(53) Kiss, G. *J. Catal.* **2003**, *217*, 127.
(54) Moodley, D. J.; van de Loosdrecht, J.; Saib, A. M.; Overett, M. J.; Datye, A. K.; Niemantsverdriet, J. W. *Appl. Catal. A Gen.* **2009**, *354*, 102.
(55) Bae, J. W.; Kim, S.; Park, S.; Prasad, P. S. S.; Lee, Y.; Jun, K. 2009, 3228.
(56) Park, S.-J.; Bae, J. W.; Lee, Y.-J.; Ha, K.-S.; Jun, K.-W.; Karandikar, P. *Catal. Commun.* **2011**, *12*, 539.
(57) Balakrishnan, N.; Joseph, B.; Bhethanabotla, V. R. *Appl. Catal. A Gen.* **2013**, *462*−*463*, 107.
(58) Peña, D.; Griboval-Constant, A.; Diehl, F.; Lecocq, V.; Khodakov, A. Y. *ChemCatChem* **2013**, *5*, 728.
(59) Chambrey, S.; Fongarland, P.; Karaca, H.; Piché, S.; Griboval-Constant, A.; Schweich, D.; Luck, F.; Savin, S.; Khodakov, A. Y. *Catal. Today* **2011**, *171*, 201.

(60) Sadeqzadeh, M.; Hong, J.; Fongarland, P.; Curulla-Ferré, D.; Luck, F.; Bousquet, J.; Schweich, D.; Khodakov, A. Y. *Ind. Eng. Chem. Res.* **2012**, 11955.
(61) Schanke, D.; Hilmen, A.; Bergene, E.; Kinnari, K. *Catal. Lett.* **1995**, *34*, 269.
(62) Schanke, D.; Hilmen, A.; Bergene, E. *Energy Fuels* **1996**, *10*, 867.
(63) Krishnamoorthy, S.; Tu, M.; Ojeda, M. P.; Pinna, D.; Iglesia, E. *J. Catal.* **2002**, *211*, 422.
(64) Sehested, J.; Carlsson, A.; Janssens, T. V. W.; Hansen, P. L.; Datye, A. K. *J. Catal.* **2001**, *197*, 200.
(65) Richardson, J. T.; Crump, J. G. *J. Catal.* **1979**, *57*, 417.
(66) Neouze, M.-A. *J. Mater. Sci.* **2013**, *48*, 7321.
(67) Xin, H. L.; Mundy, J. A.; Liu, Z.; Cabezas, R.; Hovden, R.; Kourkoutis, L. F.; Zhang, J.; Subramanian, N. P.; Makharia, R.; Wagner, F. T.; Muller, D. A. *Nano Lett.* **2012**, *12*, 490.
(68) Wickman, B.; Seidel, Y. E.; Jusys, Z.; Kasemo, B.; Behm, R. J. *ACS Nano* **2011**, *5*, 2547.
(69) Seidel, Y.; Jusys, Z.; Wickman, B.; Kasemo, B.; Behm, R. J. *ECS Trans.* **2010**, *25*, 91.